JOURNAL OF GEOPHYSICAL RESEARCH, VOL. 113, D14S23, doi:10.1029/2007JD009649, 2008

Evidence for the impact of aerosols on the onset and microphysical properties of rainfall from a combination of satellite observations and cloud-resolving model simulations

Wesley Berg,[1] Tristan L'Ecuyer,[1] and Susan van den Heever[1]

Received 28 November 2007; revised 26 February 2008; accepted 16 April 2008; published 25 June 2008.

[1] Satellite rainfall estimates from the Tropical Rainfall Measuring Mission's (TRMM) precipitation radar (PR) and microwave imager (TMI) exhibit large differences off the coast of China and extending east across the North Pacific storm track. These differences suggest the modification of precipitating clouds on a large scale with potentially important implications for seasonal rainfall estimates. Coincident TRMM/CloudSat observations for a case from 3 April 2007 show striking differences in both rain area and rainfall intensity from the TMI, PR, and CloudSat retrievals. Observations from the 94-GHz CloudSat radar, which is highly sensitive to the onset of rain, confirm the presence of widespread light rain/drizzle containing relatively small drops below the ~17 dBZ PR detection threshold. For pixels with reflectivities above the PR detection threshold, large differences are present in the satellite rain intensity estimates, which are consistent with either a decrease in the mean drop size, an increase in ratio of cloud water to rainwater, or both. To explore the potential link between aerosols and the observed changes in the observed cloud microphysics, idealized cloud-resolving model (CRM) simulations initialized for the 3 April 2007 case are performed. The model results are generally consistent with the observations indicating high aerosol concentrations leading to an overall increase in the ratio of cloud water to rainwater for developed systems, as well as a delay in the onset of warm rain. The simulations also show an initial decrease in the mean raindrop size, although larger drops develop later leading to an overall increase in the total rainfall accumulation. On the basis of the combination of observations and CRM simulations, therefore, it is hypothesized that the observed differences may be due to an increase in the ratio of cloud water to rainwater leading to an overestimate in rain intensity by the CloudSat/TMI retrievals and/or a decrease in the mean drop size leading to an underestimate by the PR retrieval.

Citation: Berg, W., T. L'Ecuyer, and S. van den Heever (2008), Evidence for the impact of aerosols on the onset and microphysical properties of rainfall from a combination of satellite observations and cloud-resolving model simulations, *J. Geophys. Res.*, *113*, D14S23, doi:10.1029/2007JD009649.

1. Introduction

[2] The transition from cloud water to precipitation is a critical process central to both the atmospheric energy budget and water cycle since it affects the rate at which water is removed from the atmosphere. Recently, a comparison of precipitation products from the Tropical Rainfall Measuring Mission (TRMM) has revealed new evidence for the suppression/modification of precipitation in warm clouds in the aerosol-rich East China Sea [*Berg et al.*, 2006]. While many other studies have investigated the role of aerosols in suppressing and/or modifying the microphysical properties of clouds [*Rosenfeld and Lensky*, 1998; *Rosenfeld*, 1999; *Ishizaka et al.*, 2003; *Givati and Rosenfeld*, 2004; *Matsui et al.*, 2004; *Khain et al.*, 2005; *van den Heever et al.*, 2006; *Jiang et al.*, 2006; *Xue and Feingold*, 2006; *Zhao et al.*, 2006; *Carrio et al.*, 2007; *van den Heever and Cotton*, 2007], studies of the impact of such cloud modification on satellite rainfall observations are limited [*Lin et al.*, 2006]. Because satellites provide the only source of rainfall observations over much of the globe, understanding the impact of aerosols on clouds and precipitation is important not only for estimating rainfall from satellite data, but also for understanding the climatological impact of aerosols on rainfall processes.

[3] *Berg et al.* [2006] hypothesized that the presence of high sulfate concentrations over the East China Sea may lead to the frequent occurrence of high liquid water content clouds with either no precipitation or light rainfall with

[1]Department of Atmospheric Science, Colorado State University, Fort Collins, Colorado, USA.

0148-0227/08/2007JD009649$09.00

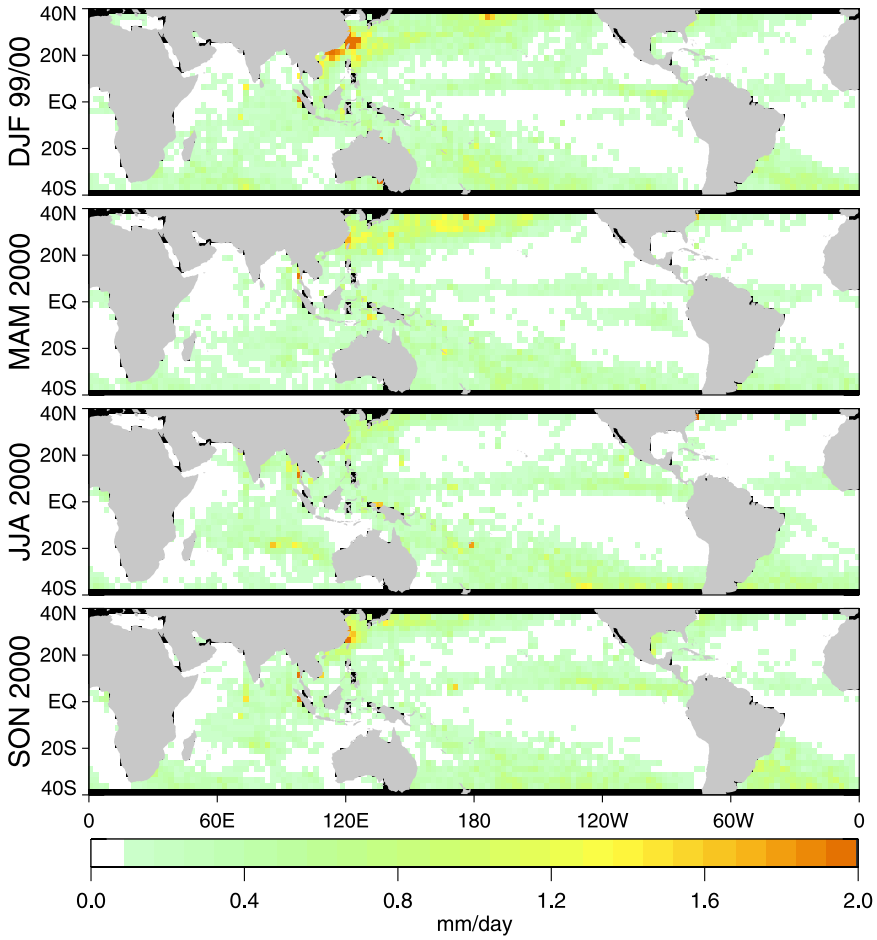

Figure 1. Seasonal mean differences in rainfall detection between the active (PR) and passive (TMI) sensors on board TRMM based on pixel matched data. Only those pixels where rainfall was detected by the TMI 2A12 retrieval, but not by the PR 2A25 retrieval are included.

small drops below the ~17 dBZ detection threshold of the TRMM PR. Figure 1 shows the impact of these differences in rainfall detection between the PR and TMI on seasonal rainfall totals over the tropical oceans for a 1-year period. As described by *Berg et al.* [2006], only those pixels identified as raining by TMI, but not by PR, are included in the totals shown in Figure 1. While clouds exhibiting these characteristics appear throughout the Tropics, they occur most frequently over the East China Sea and to the east along the midlatitude North Pacific storm track. The largest signal occurs right off the China coast during December, January, and February (DJF) 1999/2000, although it is present during the other seasons, particularly March, April, and May (MAM) where it is dispersed eastward along the storm track. It should be noted that the ~2 mm/d maximum shown in Figure 1 along the coast of China during DJF 1999/2000 is primarily due to TMI detecting rain approximately twice as frequently as PR, which in turn accounts for almost 50% of the total estimated TMI rainfall. As *Berg et al.* [2006] point out, however, it is not known whether the TMI or PR estimates are closer to the "true" rainfall. As such, the associated uncertainty in the total seasonal mean rainfall estimates in this region could be as much as 100%, with lesser, but still significant impacts further from the coast as well as during other seasons.

[4] Figure 2 shows corresponding mean sulfate aerosol optical depths from the Spectral Radiation-Transport Model for Aerosol Species (SPRINTARS) [*Takemura et al.*, 2000, 2002, 2005]. On the basis of the SPRINTARS model it is clear that over the ocean regions shown in Figure 2, the highest concentrations of sulfate aerosols regularly occur over the East China Sea. While there appears to be a relationship between the differences in satellite rainfall detection shown in Figure 1 and the sulfate aerosols shown in Figure 2, seasonal differences between the two plots suggest that changes in the environmental conditions and the synoptic forcing play a significant role as well.

[5] Although the differences in rainfall detection between the TRMM PR and TMI point to a modification of the drop size distribution (DSD), the lack of any signal below the ~17 dBZ threshold of the PR makes it difficult to verify this hypothesis. The recent launch of CloudSat in May of 2006 provides complementary information related to the onset of precipitation since the minimum detectable signal of its 94-GHz cloud profiling radar (CPR) is −30 dBZ making it sensitive to clouds, drizzle, and light rainfall [*Austin and Stephens*, 2001; *L'Ecuyer and Stephens*, 2002]. Because TRMM has an orbital inclination of 35° it regularly crosses the ground track of the polar-orbiting CloudSat/A-Train constellation (98° inclination) providing between

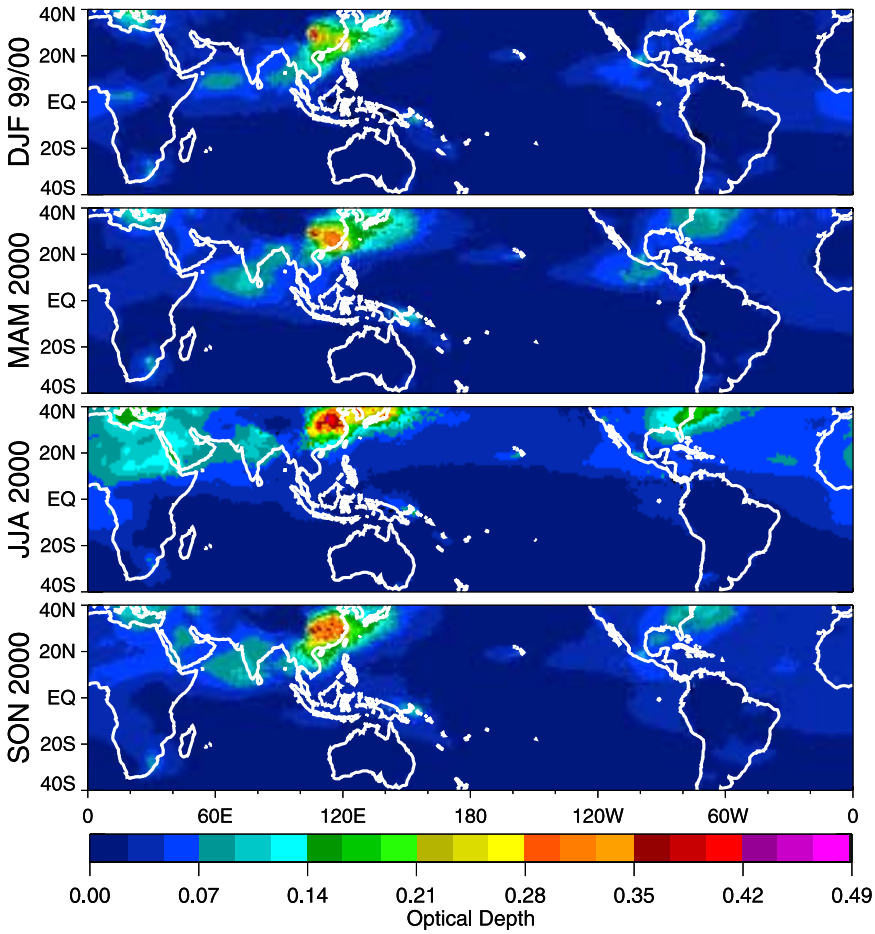

Figure 2. Seasonal mean sulfate aerosol optical depth from the Spectral Radiation-Transport Model for Aerosol Species (SPRINTARS) model.

two and three coincident overpasses every day that intersect within five minutes of each other.

[6] Two scenes with coincident CloudSat/TRMM observations are examined in detail here. The first scene, from 2 December 2006, is shown to demonstrate the complimentary information provided for a case where rain estimates from the three satellite rain sensors, including PR, TMI, and the CloudSat Cloud Profiling Radar (CPR), are in relatively good agreement. The second case, from 3 April 2007, corresponds to a high aerosol warm rain scene that, like the case discussed by *Berg et al.* [2006], exhibits large differences in the location and intensity of rain from the satellite sensors. Although the synoptic conditions play a critical role on the resulting cloud microphysics and the subsequent influence of aerosols [*Matsui et al.*, 2004, 2006; *Kaufman et al.*, 2005], limited availability of coincident TRMM/CloudSat observations of warm rain systems makes it impossible to identify cases that differ only with respect to the presence and/or concentration of sulfate aerosols. To attempt to establish the link between aerosols and microphysical changes, therefore, idealized CRM simulations corresponding to the observational case are used to determine if increases in cloud condensation nuclei (CCN) concentrations produce results that are consistent with the observed differences. It should be noted that both the observational analyses and model simulations involve numerous factors that cannot be fully controlled/accounted for when analyzing such a limited number of cases. Consistency between them, on the other hand, significantly strengthens the case beyond what can be made from either source independently. Furthermore, as Figure 1 clearly indicates, the observed differences in rainfall detection are not limited to a few cases, but are a frequent occurrence in this region. As a result, they have important ramifications both for estimating rainfall from satellites and for understanding the climatological impacts of aerosols on the hydrologic cycle.

2. Data

[7] The observational evidence presented in this paper for the modification of clouds by aerosols relies heavily on an understanding of how differences between passive (i.e., radiometer) and active (i.e., radar) sensors operating at different frequencies (i.e., 13.8-GHz TRMM PR versus 94-GHz Cloudsat) respond to nonprecipitating versus precipitating clouds, as well as to changes in the rainfall DSD. The arguments that follow center on the use of a unique combination of satellite data sets from the first precipitation radar, TRMM's 13.8-GHz PR [*Kummerow et al.*, 1998, 2000], and the first cloud radar, CloudSat's 94-GHz CPR [*Stephens et al.*, 2002] flown in space. Individually, active sensors offer the advantage of providing information on the

vertical structure of clouds and rainfall, but together the different frequencies of the PR and CPR provide an even more powerful tool by virtue of differences in their sensitivity. Rainfall estimates from the TRMM PR, for example, are primarily based on backscattered radiation from raindrops that nominally increases with the sixth moment of the raindrop size distribution [*Iguchi et al.*, 2000]. As a result, the PR rain rate estimates, like those of conventional ground-based radar systems, are derived primarily from the largest raindrops in the sample volume that constrain an assumed DSD by fixing the number of particles in the large particle tail of the distribution. It is perhaps not surprising, then, that the dominant source of uncertainty in PR rainfall estimates is the shape of the assumed DSD. While the assumed DSD may be adjusted in moderate to heavy rainfall when the PR experiences sufficient attenuation to provide a reliable estimate of the path-integrated attenuation (PIA), the attenuation of the PR signal is negligible for light rain. Most relevant to the issue of rainfall detection is the sensitivity of the PR, which has a minimum detectable signal of ~17 dBZ, making the PR insensitive to cloud water or light rainfall although the minimum detectable rainfall rate is a function of DSD and, therefore, cannot be precisely specified.

[8] For CloudSat, strong attenuation at 94 GHz from drizzle and light rain makes it possible to exploit fundamentally different physical principles to estimate rainfall intensity than those adopted for the PR. This attenuation forms the basis of a preliminary rainfall detection and intensity estimation algorithm based primarily on the PIA that has recently been developed for CloudSat (J. M. Haynes et al., Rainfall retrieval over the ocean using spaceborne high-frequency cloud radar, submitted to *Journal of Geophysical Research*, 2008). The technique is based on the fact that in clear skies the backscatter from the ocean's surface is determined, to first order, by surface wind speed and SST. The PIA in a raining scene can, therefore, be estimated as the difference between the observed surface return and the equivalent clear-sky value based on wind speed and SST. Haynes et al. (submitted manuscript, 2008) employ Monte Carlo simulations that include both attenuation and multiple-scattering effects to relate this observed PIA to rainfall rate using a rigorous model that includes vertical profiles of cloud and rainfall from CRM simulations, an assumed Marshall-Palmer distribution of raindrops [*Marshall and Palmer*, 1948], discrete dipole approximation (DDA) calculations of the scattering properties of dendritic snow crystals, and a complete model of the dielectric properties of the melting layer based on profiles of humidity and temperature.

[9] Unlike backscatter, attenuation is primarily sensitive to the condensed water mass in the atmosphere making it less susceptible to the details of the raindrop size distribution [*Matrosov*, 2007], but introduces additional sensitivity to nonprecipitating cloud water in its field of view. It should be noted that this would not be true for a CPR rain rate algorithm that relates reflectivity to rain rate, after application of a suitable attenuation correction. It is also important to note that while the CPR has a spatial resolution of approximately 1.5 km, it only points in a nadir direction, thus providing a single vertical profile along the flight direction. On the other hand, PR is a scanning radar that covers an approximately 250 km swath, although at a lower spatial resolution of approximately 5 km.

[10] Passive microwave observations from the TRMM microwave imager (TMI), which makes observations at frequencies of 10.65, 19.35, 21.3, 37.0, and 85.5 GHz, are also very sensitive to attenuation/emission from both clouds and rain. Over oceans, the low emissivity of the surface at these frequencies provides a radiometrically cold background against which the more emissive hydrometeors appear warm. Because TMI makes observations at multiple frequencies and polarizations it is sensitive to emission from clouds, light rain, and even heavy rain since the signal in the low-frequency channels does not saturate even for very large amounts of liquid water. A disadvantage of the TMI is its relatively low spatial resolution, which varies from ~5 km for the 85.5-GHz channels down to ~50 km for the 10.65-GHz channels. Compared to the radar backscatter signal from PR and CPR the impact of changes in the DSD is significantly less, although not negligible, for both the TMI brightness temperatures and the CPR attenuation. As a result, there is a strong correlation between increases in brightness temperature and the total liquid water path (LWP) from both clouds and rain. Note that the subsequent use of the designation LWP is in reference to the total liquid water path while CWP is used to refer to cloud liquid water path and RWP to refer to rain liquid water path.

[11] Differences in the instrument operating principles, such as those mentioned above, will manifest themselves in the scene interpretation. For instance, a decrease in the characteristic size of raindrops will manifest itself as a significant reduction in the PR backscatter and thus the rain rate, but will have a much smaller impact on the rain estimates from TMI or the attenuation-based rain estimates from CPR. On the other hand, for a given amount of rainwater, an increase in the ratio of nonprecipitating cloud water to rainwater will have little impact on the PR, but would be misinterpreted as more intense rainfall by the attenuation/emission-based CPR and TMI algorithms.

3. Coincident Observations From TRMM and CloudSat

[12] Given the physical differences in the three rainfall sensors from TRMM and CloudSat, it is important to understand how the resulting observations compare in a typical case. Rainfall estimates corresponding to a coincident overpass from TRMM and the CloudSat/A-Train constellation are shown in Figure 3 for a case from 2 December 2006 located to the east of Japan. In Figure 3a geostationary infrared imagery show the large-scale cloud field with the selected region containing coincident TRMM/CloudSat observations indicated by the red box located at 156–166°E and 29–39°N. Rainfall estimates from the TRMM PR based on the 2A25 retrieval algorithm [*Iguchi et al.*, 2000] and from TMI based on the 2A12 retrieval algorithm (i.e., GPROF) [*Kummerow et al.*, 2001] are shown for this 10° × 10° region in Figures 3b and 3c with the nadir track of the nonscanning CPR is indicated by the black line extending from north to south. For the purposes of comparing the PR and TMI rainfall estimates, the high-resolution (~5 km) PR rain rates have been averaged to match the larger (~25 km) TMI field of view (FOV) with the resulting

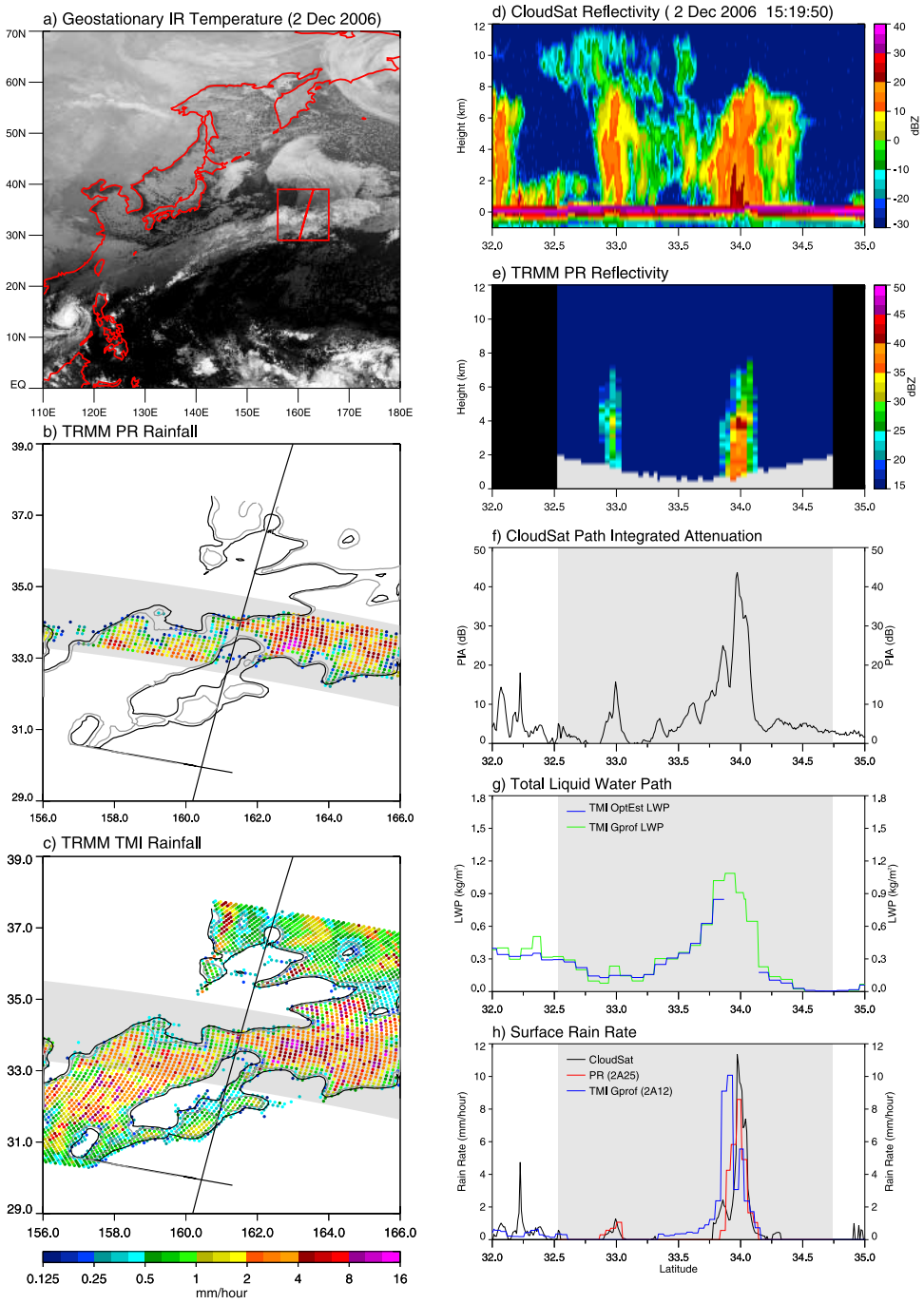

Figure 3. A comparison of satellite observed and retrieved quantities for a coincident TRMM/CloudSat overpass from 2 December 2006 at 1520 UT. Plots include (a) large-scale infrared imagery from the Japanese geostationary multifunctional transport satellite (MTSAT-1R) with the selected region from 29–39°N and 156–166°E indicated by the red box, (b) PR 2A25 rainfall estimates over the selected region averaged to TMI spatial resolution, and (c) TMI 2A12 rainfall estimates with the PR swath indicated by a gray background. Liquid water path contours of 0.3 (black) and 0.4 (gray) kg/m^2 are plotted over the PR and TMI rainfall estimates. The remaining panels correspond to the CloudSat ground track indicated by the black line in Figures 3b and 3c. They include attenuation-corrected reflectivity profiles from (d) CloudSat and (e) PR, (f) CloudSat PIA, (g) liquid water path from TMI, and (h) surface rain rate estimates from CloudSat, PR, and TMI.

area-averaged PR rain estimates shown in Figure 3b. The light gray shaded region in these plots indicates the coverage of the PR swath. In addition, TMI-derived LWP contours corresponding to 0.3 and 0.4 kg/m^2 are plotted over the top of both the PR and TMI rain rate estimates shown in Figures 3b and 3c. The LWP estimates were computed from the TMI brightness temperatures using an optimal estimation (OE) retrieval developed by *Elsaesser and Kummerow* [2008] that is completely independent of the 2A12 algorithm. A visual comparison of coincident rain rate estimates from the active (PR) and passive (TMI) sensors indicates excellent agreement in both the rain area and the rain intensities for this case. The rain area corresponds closely to the 0.3 kg/m^2 LWP contour and the maximum rain rates exceed 8 mm/h for both sensors.

[13] Observed and retrieved quantities from TRMM and CloudSat along the intersection of the satellite ground tracks are shown in Figures 3d–3h. Vertical profiles of attenuation-corrected reflectivities from CloudSat and PR are shown in Figures 3d and 3e, respectively. The CloudSat PIA, shown in Figure 3f, responds primarily to absorption by liquid hydrometeors and is derived by differencing the observed surface return from the expected clear-sky value. For clear-sky scenes, differences between the observed and expected surface return, computed from the surface wind speed and SST, generally agree to within ±1dB (Haynes et al., submitted manuscript, 2008). Two different LWP estimates from TMI are shown in Figure 3g including the OE retrieval and the simple estimate used in the GPROF rainfall algorithm [*Kummerow et al.*, 2001] for rain/no rain determination. The GPROF LWP is computed from the TMI brightness temperatures (TBs) using the simple relationship:

$$\mathrm{LWP} = 0.399635^* \log(280.0 - \mathrm{TB}_{22\mathrm{V}}) - 1.40692^* \times \log(280.0 - \mathrm{TB}_{37\mathrm{V}}) + 4.299$$

where $\mathrm{TB}_{22\mathrm{V}}$ and $\mathrm{TB}_{37\mathrm{V}}$ are the vertically polarized brightness temperatures (in Kelvin) at 22 and 37 GHz, respectively. While the two independent LWP retrievals agree quite well, the OE retrieval fails over the area of deep convection where scattering by ice hydrometeors significantly depresses the TMI TBs. It is likely that the GPROF LWP estimates corresponding to this area of deep convection are unreliable as well. Finally, the rain rate estimates from the CPR are from the attenuation-based retrieval described in the data section while the PR and TMI estimates are from the TRMM 2A25 and 2A12 retrievals, respectively.

[14] The rain estimates along the CloudSat transect from the three sensors, shown in Figure 3h, agree quite well in both the intensity and area identified as raining. The higher spatial resolution and sensitivity of the CPR shows some relatively isolated areas of light rain not detected by one or both of the TRMM sensors, but overall the agreement between this diverse set of sensors and associated algorithms is quite good. There are some differences particularly with respect to the location of the TMI rain features relative to the other two sensors, however, these may be attributable to mismatches in space and/or variations in sensor resolution, which ranges from ~1.5 km for CloudSat to ~5 km for PR and ~25 km for TMI. For example, the rainfall peak near 34.0°N in the CloudSat and PR estimates lies directly between two TMI scans separated by nearly 13.5 km, thus leading to an apparent disagreement in the location of the rain cell.

[15] The good agreement of the rainfall estimates suggests that the underlying DSD assumption in all three retrieval algorithms provides a reasonable representation of the true distribution since each sensor responds very differently to changes in DSD. Both the CPR and TMI 2A12 algorithms assume an exponential Marshall-Palmer distribution [*Marshall and Palmer*, 1948] while the PR retrieval uses a similar gamma distribution that gives rain rates within ~10% of the Marshall Palmer value for light to moderate convective pixels. Any significant deviation from the assumed DSDs will, therefore, affect the various retrievals differently leading to significant differences in the estimates of rain intensity.

4. Investigating Disparities Within a Polluted Air Mass

[16] While the rainfall estimates from the 2 December 2006 case shown in Figure 3 indicate very good agreement between the diverse TRMM and CloudSat rainfall sensors and their associated retrieval algorithms, as Figure 1 indicates, this is frequently not the case off the coast of China. On the basis of differences in rainfall detection in this region, *Berg et al.* [2006] hypothesized that high concentrations of sulfate aerosols lead to the formation of clouds with high LWP and possibly light rain below the PR sensitivity (~17 dBZ). Examining coincident overpasses from TRMM and CloudSat, we have identified several high aerosol cases exhibiting substantial differences in both the rain area and rainfall intensity from the three satellite sensors.

[17] The results from one of these cases corresponding to 3 April 2007 is shown in Figures 4 and 5. Figure 4a shows the large-scale geostationary IR imagery for this case, with the selected region containing coincident TRMM/CloudSat observations indicated by the red box/line located at 138–148°E and 26–36°N. As the IR imagery in Figure 4a indicates, this region is downwind of the axis of a trough, easily identified by the broad region of cloudiness, moving directly across mainland China over the aerosol source region shown in Figure 2. Animations of geostationary IR imagery (not shown) confirm the presence of this wave pattern over the preceding days with the trough digging southward and intensifying as the entire trough-ridge pattern moves eastward transporting aerosol rich clouds northeast across the Pacific. It should be noted that while these meteorological conditions are very different than those associated with the 2 December 2006 case, the intent is not to directly compare the two cases. Instead, the goal is to determine if observed differences in the 3 April 2007 case, and by association the corresponding changes in the cloud microphysical properties, are consistent with high concentrations of sulfate aerosols and thus large numbers of cloud condensation nuclei. In this case, observations of aerosol optical depth from the Moderate Resolution Imaging Spectroradiometer (MODIS) in Figure 4b as well as modeled sulfate aerosol optical depths from SPRINTARS in Figure 4c both indicate the presence of high aerosol concentrations.

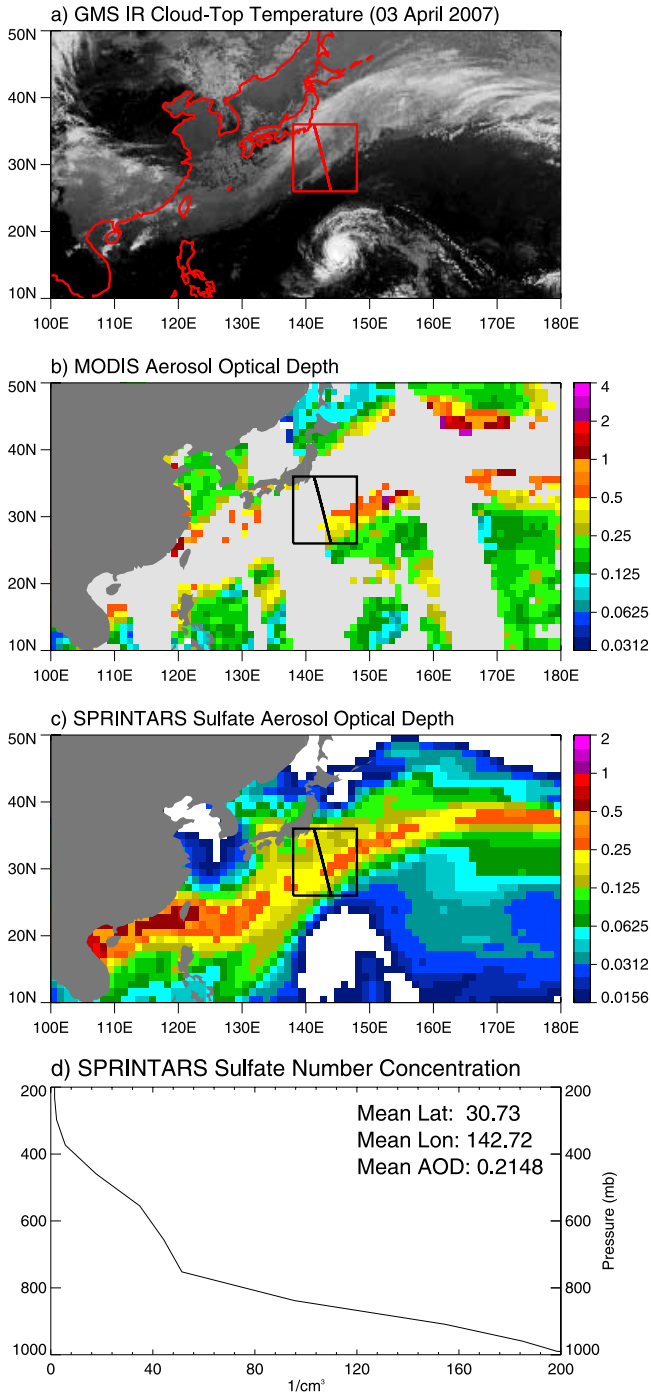

Figure 4. Cloud and aerosol features from 3 April 2007 over the northwest Pacific including (a) infrared imagery from the Japanese MTSAT-1R satellite, (b) aerosol optical depth from MODIS, (c) sulfate aerosol optical depth from SPRINTARS, and (d) the vertical profile of sulfate number concentration from SPRINTARS. The selected region along with the CloudSat ground track are indicated by the red/black box in Figures 4a–4c.

While aerosol retrievals from MODIS are not available over the cloud-covered regions shown in Figure 4a, the observations support the model results, which indicate a plume of high aerosols concentrations over the selected region. The SPRINTARS model provides vertical distributions of aerosol species over both clear and cloudy regions, as opposed to satellite-based aerosol retrievals such as those from MODIS that are limited to clear-sky scenes only. Figure 4d shows the mean SPRINTARS vertical profile of sulfate aerosol number concentration over the selected region, with a mean aerosol optical depth of 0.2148. Browse images of the total attenuated backscatter (not shown) from the A-Train's Cloud-Aerosol Lidar and Infrared Pathfinder Satellite Observations (CALIPSO) also indicate a clearly identifiable layer of aerosols between ~2.5–4.0 km within a clear-sky region to the south of where the TRMM/CloudSat ground tracks intersect.

[18] Figure 5 shows a comparison of the same observed and retrieved quantities from TRMM and CloudSat as shown in Figure 3 for the 2 December 2006 case. Unlike Figure 3, however, the PR and TMI rainfall estimates are shown in Figures 5a and 5b with histograms of these coincident estimates shown in Figure 5c. The CloudSat reflectivity values, shown in Figure 5d, indicate relatively shallow clouds north of 30.8°N with cloud tops at or near the freezing level, which is around 4 km on the basis of NCEP reanalysis data. While slightly deeper clouds over the southern part of the PR scan may involve some ice microphysics, CloudSat indicates relatively warm cloud processes over much of the region of coincident TRMM/CloudSat observations.

[19] As Figures 5a and 5b show, this case exhibits broad disagreement between the PR and TMI rain retrievals in both the rain area as well as the rainfall intensity. Focusing along the section of the CloudSat ground track intersecting the narrow PR swath reveals that while the TMI retrieval detects rain across the entire inner swath, the PR indicates only partial rain coverage. In addition, along the CloudSat track the intensity of the rain rate estimates from the two sensors differs significantly, with TMI showing a broad area of rain over 1 mm/h while only a single PR pixel along the transect exceeds that value. A closer inspection of observed and retrieved quantities from TRMM and CloudSat along the intersection of the satellite ground tracks provides some insight into the reasons for these differences. As noted by *Berg et al.* [2006], the root of these discrepancies lies in the numerous assumptions required to both detect and infer rainfall intensity from the three sensors. To better understand the differences in algorithm behavior in this case it is, therefore, important to look at fields more closely related to the raw observations, and thus less impacted by assumptions as is the case for the rain retrieval algorithms. Similar to Figure 3, observed and retrieved quantities from CloudSat, PR, and TMI are shown in Figures 5d–5h along the CloudSat transects. Both the CloudSat and TMI retrievals indicate rain across most of an approximately 200 km swath from 30.25°N to 32.2°N while PR only detects light rain along a small portion of this region. This is consistent with the large-scale differences in rain area shown in Figures 5a and 5b. Although there are significant differences in rain intensity between CloudSat and TMI across this region, this is likely due in large part to the dramatic differences in spatial resolution (i.e., 1.5 versus 25 km) combined with the relatively high spatial variability of these rain cells, as indicated in Figure 5d. While the ~17 dBZ minimum detectable signal of the PR means that it cannot detect

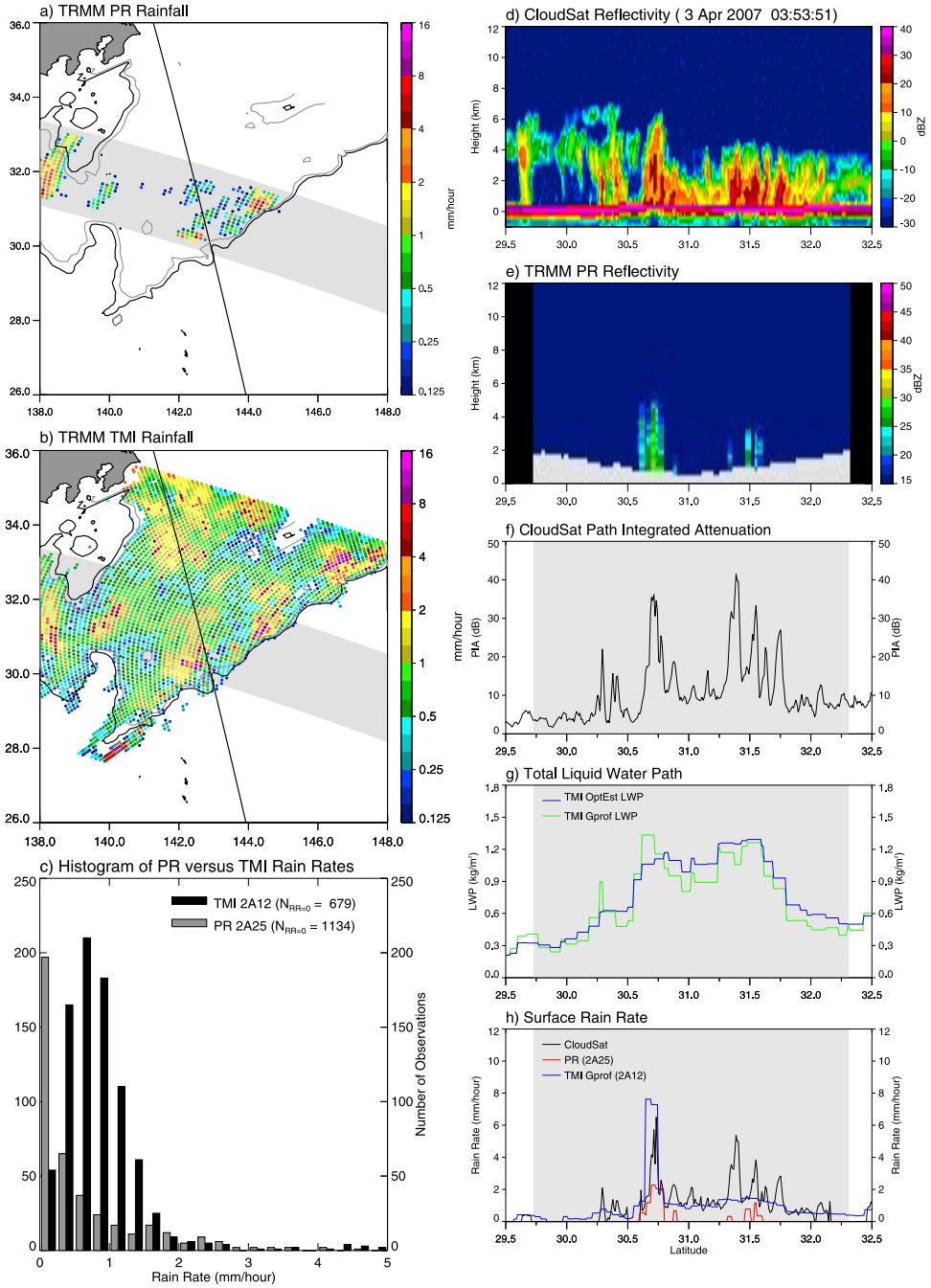

Figure 5. A comparison of satellite observed and retrieved quantities for a coincident TRMM/CloudSat overpass from 3 April 2007 at 0345 UT over the selected region from 26–36°N and 138–148°E. Plots include (a) PR 2A25 rainfall estimates over the selected region averaged to TMI spatial resolution, (b) TMI 2A12 rainfall estimates with the PR swath indicated by a gray background, and (c) histograms of the matched PR and TMI rain rate estimates. Liquid water path contours of 0.3 (black) and 0.4 (gray) kg/m^2 are plotted over the PR and TMI rainfall estimates. The remaining panels correspond to the CloudSat ground track indicated by the black line in Figures 5a and 5b. They include attenuation-corrected reflectivity profiles from (d) CloudSat and (e) PR, (f) CloudSat PIA, (g) liquid water path from TMI, and (h) surface rain rate estimates from CloudSat, PR, and TMI.

clouds and light rain [*Schumacher and Houze*, 2000], the CPR is highly sensitive to the transition from cloud to rain. The pixels identified as raining in Figure 5h have all been flagged as rain certain with near surface attenuation-corrected reflectivity values above 0 dBZ (Haynes et al., submitted manuscript, 2008). As a result, CloudSat provides compelling evidence that the differences in rain area between PR and TMI in Figures 5a and 5b are likely due to drizzle and/or light rain that is identified as raining by the TMI retrieval algorithm, but falls below the PR detection threshold.

[20] Identifying a unique physical explanation for the substantial differences in rainfall intensity from the various sensors is more challenging. The fact that the radar reflectivities vary as a function of the sixth power of the drop diameter makes them very sensitive to changes in the DSD. For the CPR, however, Mie theory calculations for Marshall-Palmer distributions of raindrops indicate that the sensitivity of the observed reflectivities to changes in drop size decreases considerably for distributions with a mean diameter above ~0.3 mm [*Kollias et al.*, 2007]. As a result, attenuation-corrected CPR reflectivities for the intense rain cells in both the 2 December 2006 case and the 3 April 2007 case appear comparable, even though the rain rate estimates vary considerably. Unlike the 2 December 2006 case, where the rainfall estimates showed excellent agreement, the differences in the rain estimates suggest that the actual microphysical properties of the observed cloud differ significantly from underlying DSD assumptions in the three retrieval algorithms. As mentioned previously, the CPR and TMI 2A12 algorithms assume an exponential Marshall-Palmer distribution [*Marshall and Palmer*, 1948] while the PR retrieval uses a similar gamma distribution that gives rain rates within ~10% of the Marshall-Palmer value for light to moderate convective pixels. Any significant deviation from the assumed DSDs will, therefore, affect the various retrievals differently leading to significant differences in the estimates of rain intensity.

[21] Both the rain cells with nonzero PR reflectivities (Figure 5e) have CloudSat attenuation values (Figure 5f) over 35 dB. Such a large amount of attenuation is not possible from cloud only and thus indicates a LWP consistent with significant rainfall. As mentioned previously, given that the freezing height is around 4 km in this case, the CloudSat reflectivities indicate very little or no ice aloft particularly over the northern part of the scan, thus implying primarily warm rain clouds. The LWP estimates from TMI, shown in Figure 5g, also indicate large amounts of liquid present in the precipitating regions with values in excess of 1 kg/m^2. As with the CloudSat attenuation signal, the TBs respond to absorption by both precipitating and nonprecipitating liquid hydrometeors. Such an apparent discrepancy between relatively low PR reflectivity values and the high attenuation/LWP estimates implies either large amounts of cloud water and/or a raindrop size distribution with significantly smaller drops than the typical rainfall DSDs assumed in any of these retrieval algorithms. As noted earlier, the presence of light rain in the neighboring CloudSat rainfall estimates shown in Figure 5h suggest the presence of light rain/drizzle, which supports the hypothesis of smaller drops in the raining PR footprint. Given the ~5 km size of the PR FOV, the low PR reflectivity could also be the result of a combination of drizzle and small isolated cells with somewhat larger drops. It is worth noting that while differences in spatial resolution between the sensors and/or offsets between the pixel locations could lead to disagreement at the pixel level, it seems very unlikely that this is the source of the discrepancies in this case. As Figures 5a and 5b show, the TMI/PR differences are relatively consistent over a large region, thus indicating that simply shifting the matches by a pixel in any direction is unlikely to significantly change the results.

[22] Histograms of the TMI and PR rain rates within the 10° × 10° region are shown in Figure 5c. Only raining pixels are included in the histogram bins, however, the number of nonraining pixels are indicated in the upper left corner of the plot. Also, note that the large difference for rain rates between 0.0 and 0.25 mm/h is an artifact of the averaging required to match the higher spatial resolution PR to the TMI footprints. This is because isolated PR raining pixels within the TMI FOV will lead to nonzero rain rates when averaged at the TMI resolution even though the total liquid water over the FOV is below the TMI rainfall detection threshold. For this case the histograms show dramatically more TMI rain rates over the range from 0.25 to 1.75 mm/h. In addition, there are almost twice as many PR pixels with no rain (1134) compared to TMI (679). This difference in the TMI/PR rain rate histograms is consistent with widespread light rain/drizzle mentioned previously. It is also consistent with the CloudSat rain estimates shown in Figure 5h, which indicate light rain across almost the entire PR swath. Given the substantial differences between PR and TMI rain estimates in this case, the frequent occurrence of this type of precipitating warm clouds over the East China Sea would be consistent with the rainfall detection biases shown in Figure 1. Of course the true answer may be more complicated with additional contributions possibly coming from deeper systems with ice microphysics modified by aerosols or more isolated rain clouds for example. On the basis of differences in observations of warm rain clouds in several cases, including the 3 April 2007 case and the 1 February 2000 case discussed by *Berg et al.* [2006], however, it is apparent that these warm rain clouds contribute significantly to the observed climatological differences shown in Figure 1.

5. Assessing the Impact of Aerosols From an Idealized CRM Simulation

[23] While the satellite observations for the 3 April 2007 case indicate significant differences in the microphysical properties of the clouds from the assumed values, the postulated link between aerosols and the modification of the cloud microphysics is circumstantial and difficult to separate from the impact of changes in the synoptic forcing. There is strong evidence for the presence of light rain/drizzle in the 3 April 2007 case that is below the PR sensitivity, however, it is less clear what mechanisms are leading to the large differences in the rainfall estimates from the three sensors in the heavier raining areas. Unfortunately, it is impossible to observe identical systems that vary only with regard to the concentration of sulfate aerosols. To attempt to establish the physical plausibility of this link, therefore, numerical simulations from a CRM are performed, employing a wide variation in sulfate aerosol concentrations while keeping the synoptic forcing the same. Unlike a field campaign, the location and time was determined by the availability of the coincident satellite observations, and thus corresponding detailed meteorological observations were not available. Instead, sounding information based on the National Centers for Environmental Prediction (NCEP) reanalysis were used to initialize the model. As a result, the simulations represent an idealized case that broadly corresponds to the observations. Combined with the

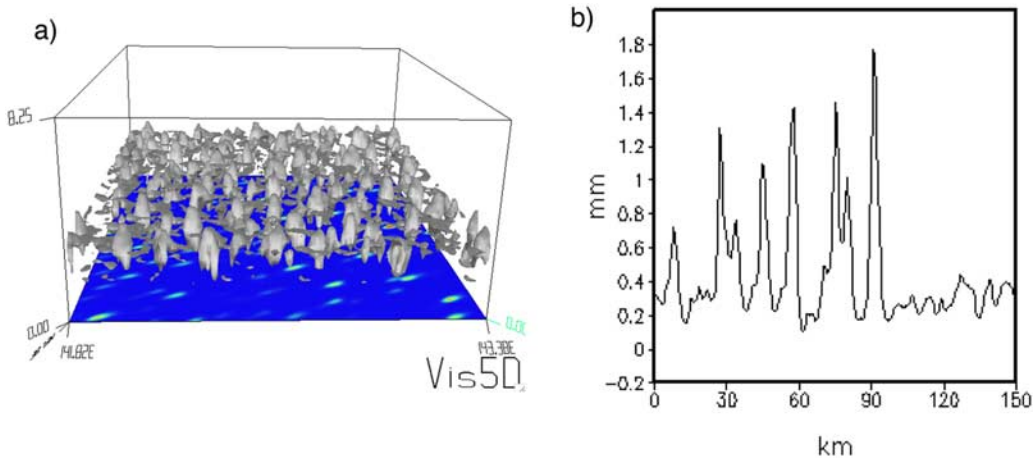

Figure 6. (a) Three-dimensional view of the cloud field at 60 min in AOD-0.2. The cloud water mixing ratio isosurface is 0.4 g/kg. Accumulated precipitation is shown in color with values ranging from 0 to 3.2 mm (blue to red). (b) The cloud liquid water path (mm) at 60 min through the middle of the domain (y = 150) for the same simulation.

lack of context of the observations within the lifecycle of the cloud, this severely limits the usefulness of quantitative comparisons between the observations and model results. Instead, the results are used in a qualitative manner to determine if changes in the simulated cloud properties associated with increased concentrations of sulfate aerosols are consistent with the observations.

[24] The Regional Atmospheric Modeling System (RAMS), a cloud-resolving model (CRM) developed at Colorado State University, was used for this study [*Pielke et al.*, 1992; *Cotton et al.*, 2003]. RAMS is a nonhydrostatic model that utilizes sophisticated microphysics, radiation, and surface schemes. A single model grid with grid spacing of 500 m in the horizontal, variable spacing in the vertical, with 10 levels falling within the first 1 km above ground level (AGL), and a spatial domain of 150 × 150 × 23 km was employed. The model was initialized horizontally homogeneously using the 0600 UTC NCEP sounding from 3 April 2007, corresponding to the location/time of the TRMM/CloudSat observations, and convection was initiated through randomized thermal perturbations to the initial potential temperature field. Periodic lateral boundary conditions were used, and the lower boundary was an ocean surface with a fixed temperature of 294 K. A time step of 5 s was utilized and the simulations were run out for 3 h.

[25] The mixing ratios and number concentrations of the various hydrometeor species were predicted through the use of a two-moment bulk microphysical scheme [*Meyers et al.*, 1997]. The model is initialized with vertical profiles of CCN, assumed to be ammonium sulfate particles, from which ambient cloud conditions are considered for the nucleation of cloud droplets from these aerosols [*Saleeby and Cotton*, 2004]. Collection is simulated using stochastic collection equation solutions [*Feingold et al.*, 1988]. For the numerical experiments performed here, the model was initialized with the vertical CCN profile obtained from the SPRINTARS model and shown in Figure 4d. The aerosol optical depth pertaining to this CCN profile is 0.2 and this simulation will subsequently be referred to as the AOD-0.2 or control run. Sensitivity tests were then conducted in which CCN concentrations of one tenth (AOD-0.02), one quarter (AOD-0.05), one half (AOD-0.1), twice (AOD-0.4), and four times (AOD-0.8) those in AOD-0.2 were used. While the initial CCN concentrations were varied in the sensitivity tests, the simulations were otherwise identical. As noted earlier, although making use of aerosol concentrations and soundings representative of actual days, the simulations are initialized horizontally homogeneously, do not include any synoptic-scale forcing, and are idealized in nature, designed to investigate potential aerosol forcing as opposed to synoptic-scale controls on the observed cloud field.

[26] The AOD-0.2 simulation initially produces a field of cumulus clouds that extend from approximately 1700 m AGL to 3000 m AGL. A three-dimensional snapshot of the simulated cloud field is shown in Figure 6a, 60 min into the AOD-0.2 run, revealing shallow cumulus clouds scattered across the entire domain. The clouds are precipitating at a rates that range from 1 to 3 mm/h for the first hour. After approximately 60 min, the cloud field becomes more stratocumulus in nature, with rain rates on the order of 0.1 to 0.5 mm/h. Although the simulations are idealized, the characteristics of the simulated cloud field including their vertical extent, rain rates, and LWP (Figure 6b) are similar to those observed by CloudSat and TMI (Figure 5).

[27] The impacts of the variations in CCN concentrations are evident in the vertically integrated cloud water, rain and total condensate fields (Figure 7). As the CCN concentrations are increased, the CWP increases (Figure 7a) and the warm rain process tends to be suppressed (Figure 7b), which is in keeping with the second indirect aerosol effect proposed by *Albrecht* [1989]. This is also consistent with the observed differences between the CloudSat/TRMM comparisons for 3 April 2007 case shown in Figure 5. The transition from a cloud field that is more cumulus in characteristics to one that is more stratocumulus around 60 min is also evident in these fields. The total LWP demonstrates the combination of the cloud and rainwater processes, with enhanced CCN concentrations being associated with reduced LWPs during the initial, more convec-

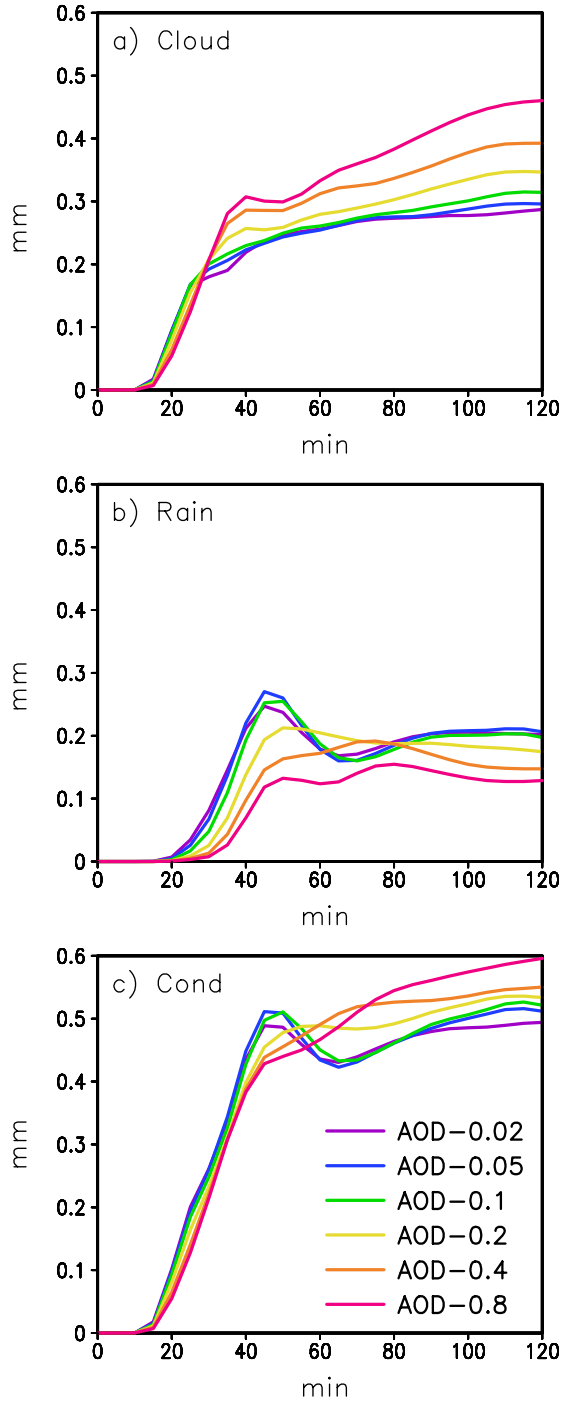

Figure 7. Time series of horizontally averaged vertically integrated (a) cloud water, (b) rainwater, and (c) total condensate for the first 2 h of simulation time for the numerical experiments described in the text.

tive cumulus stage, and greater LWPs after 60 min during the later stratocumulus stage (Figure 7c).

[28] The suppression of the warm rain process in the presence of enhanced CCN concentrations is evident during the first 60 min in the horizontally averaged accumulated surface precipitation field (Figure 8a). Eventually, however, the presence of enhanced CCN concentrations leads to the production of more rainfall at the surface. Delays in the onset of precipitation and the subsequent enhancement in accumulated precipitation associated with dynamical responses to enhanced aerosol concentrations have been observed in previous modeling studies [*Khain et al.*, 2005; *van den Heever and Cotton*, 2007]. The impact of enhanced CCN concentrations on rain and cloud water can be further analyzed by examining the ratio of the vertically integrated cloud water to LWP (Figure 8b). It is apparent from Figure 8b that rain is produced more rapidly in the cleaner cases, and that the presence of greater concentrations of CCN lead to two to three times more cloud water than rainwater throughout much of simulation, compared with the cleaner cases in which the amount of cloud water is only about 1.5 times that of the rain. It should be noted that the total rain accumulation in this case is less than 0.2 mm even though the total LWP is almost 0.5 kg/m^2. Even so, this could have significant implications for attenuation/emission-based algorithms like the CPR and TMI that rely on fixed a priori assumptions regarding the ratio of cloud water to rainwater that is independent of aerosol concentration. The delay in the onset of rain for the more polluted cases also leads to an increase in CWP prior to the development of significant rainfall. Figure 9 shows the relationship of the rainwater path (RWP) to the total LWP path during the first 40 min of the simulation. For a given RWP, the high aerosol cases exhibit a significant increase in the total LWP, and thus the cloud water.

[29] As noted above, the ability of the TMI, PR, and CPR instruments to detect rainfall is highly dependent on the hydrometeor DSD, especially for the PR. Time versus height plots are shown in Figure 10 of the horizontally averaged cloud droplet and raindrop number concentrations as well as the mean cloud and raindrop diameters for each simulation, expressed as a percentage of the control or AOD-0.2 output. The total values for each of the four output fields for the AOD-0.2 or control run are shown in row 4 of Figure 10. The values for the control run range from purple (low) to red (high) indicating that many of the large anomaly values evident early in the simulations or at higher levels are meaningless because of the low droplet concentrations and small drop sizes. It is apparent from this plot that enhanced CCN concentrations result in a greater number of cloud droplets, but these cloud droplets are smaller, which is in keeping with *Twomey*'s [1974, 1977] hypothesis. However, while a greater number of smaller cloud droplets are produced, a reduced number of raindrops are formed. These raindrops are initially smaller in the more polluted cases, but after about 50 min they become larger than in the clean cases perhaps because of a more efficient collection process when greater amounts of cloud water are available. Larger raindrops have also recently been observed for polluted conditions in simulations of moderate size coastal convective clouds [*Altaratz et al.*, 2007]. Examining the differences between the AOD-0.02 and AOD-0.2 output (top row of Figure 10), it is apparent that the lower aerosol environment shows a significant increase in the raindrop diameters initially relative to the control case, followed by a decrease on average as the system develops, emphasizing the importance of the storm life-cycle. An interesting consequence of the decrease in raindrop diameter for the lower aerosol case relative to the control is that of increased evaporation leading to a decrease

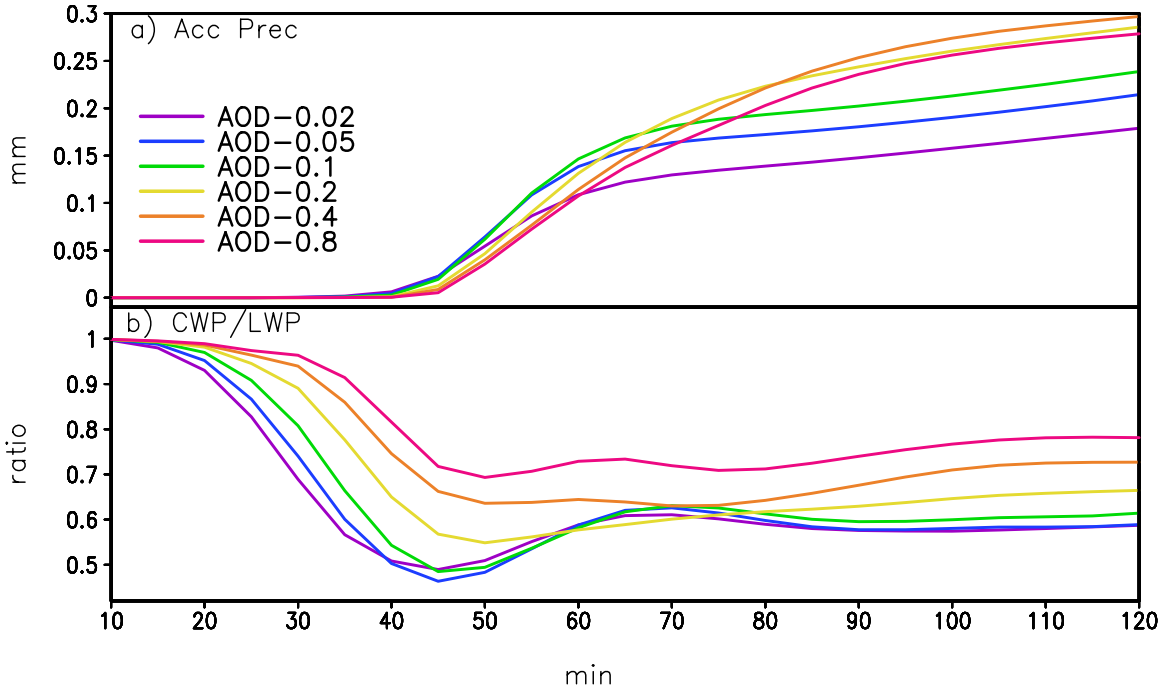

Figure 8. Time series of the horizontally averaged (a) accumulated surface precipitation (mm) and (b) vertically integrated cloud water to total LWP for the first 2 h of the simulation for the numerical experiments discussed in the text.

in the accumulated rainfall at the surface. This is apparent in plots of the rainfall mixing ratio (not shown), which indicate more rainwater aloft, but less rain at the surface due to increased evaporation for the lower aerosol case. This also explains why the model produces the seemingly contradictory results shown in Figures 7b and 8a, which indicate a higher rainwater path in the lower aerosol case, but a lower total rain accumulation relative to the control case.

[30] Both the delayed onset of rain and the large increase in the ratio of cloud water to rainwater for developed systems in the high aerosol CRM simulation cases have direct implications for the observational analyses in section 4. The increase in LWP prior to the onset of rain shown in Figure 9 suggests that the TMI retrieval may slightly overestimate the raining area because of high water content nonprecipitating clouds. The comparisons along the CloudSat ground track, however, indicate that TMI does a reasonable job in identifying the raining region for the 3 April 2007 case. In addition, the small difference in the area defined by the 0.3 and 0.4 kg/m^2 LWP contours in Figure 5a suggests that the dramatic difference in rain area between PR and TMI shown in Figures 5a and 5b is largely due to light rain not detected by PR. The quantitative rainfall estimates from the CPR and TMI are, however, very sensitive to the ratio of cloud water to rainwater. An increase in this ratio for the 3 April 2007 case consistent with the CRM simulations would result in an overestimate by the CPR and TMI retrievals due to an underestimate of the attenuation/emission from cloud water and subsequent overestimate of the attenuation/emission due to rain and, hence the inferred rainfall rate (Haynes et al., submitted manuscript, 2008). The CRM simulations also show a decrease in the number of raindrops for the polluted cases along with an initial decrease in the drop size followed by in increase in the drop size as the system develops. Depending on the stage of development of the 3 April 2007 case shown in Figure 5, this could serve to decrease/increase the observed PR reflectivities depending on whether the system is early/late in its lifecycle. Of course the CRM simulations do not allow for the possible influx of aerosols into the system, thus leading to lower aerosol concentrations as they are rained out. In addition, the rain cell located at 30.7°N in

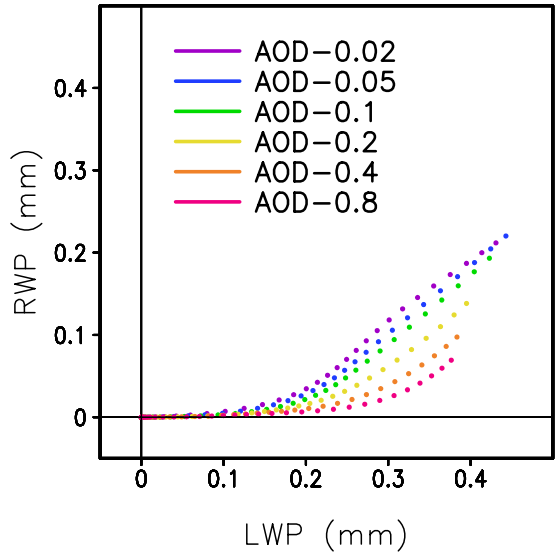

Figure 9. Relationship of the rainwater path (RWP) to the total LWP output at 1 min intervals during the first 40 min of the simulation.

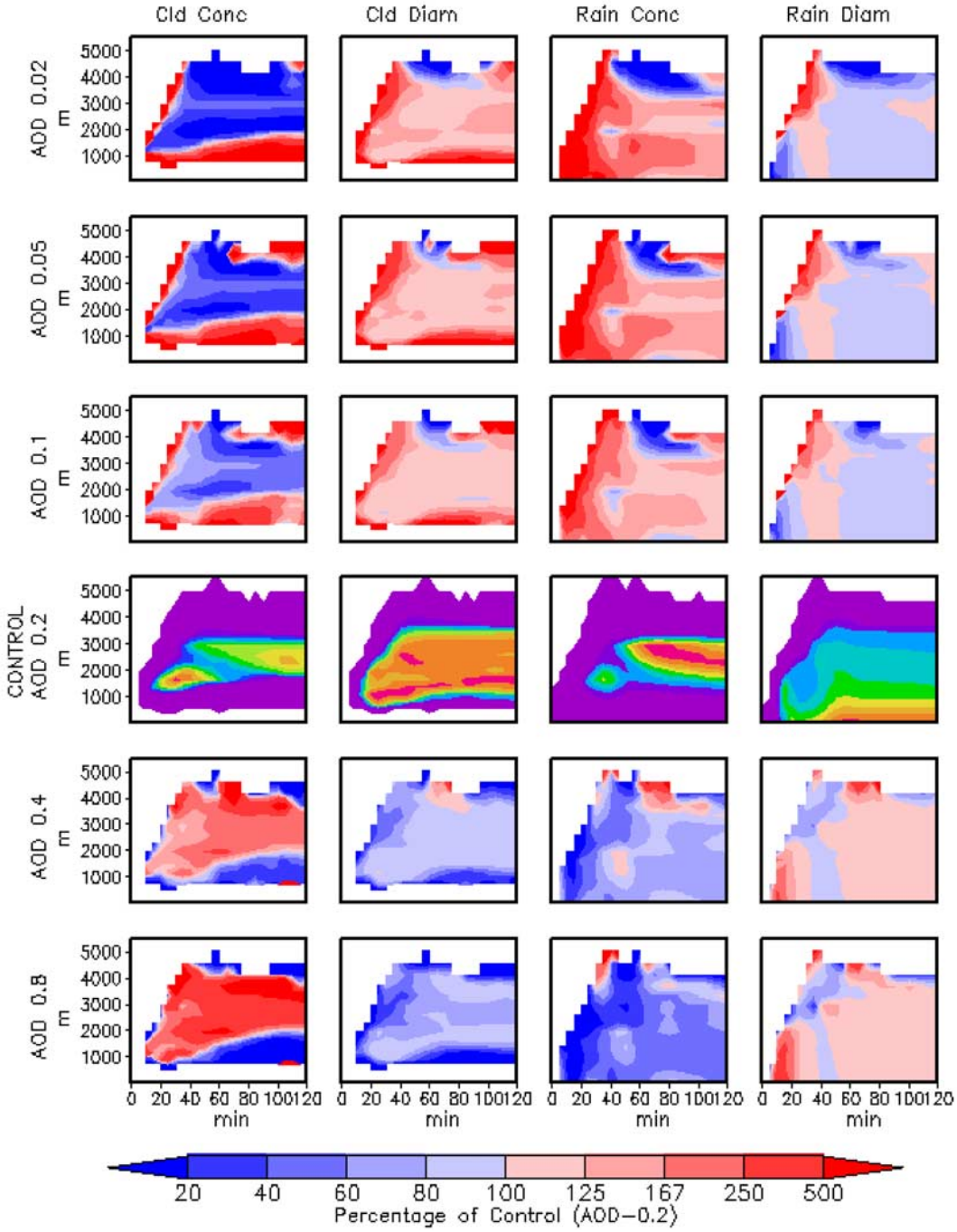

Figure 10. Time height plots of the horizontally averaged cloud droplet number concentrations (first column), mean cloud drop diameters (second column), raindrop number concentrations (third column), and mean raindrop diameters (fourth column) for the experiments (each row is a different experiment) discussed in the text, expressed as a percentage of the AOD-0.2 or control simulation. Note that for the AOD 0.2 or control run, the absolute values are shown, with values ranging from low (purple) to high (red).

Figure 5h shows significant reflectivity values above the freezing level, indicating that ice processes, which are not a factor in the simulations, may contribute to the large differences observed between the rain rate estimates. In general, however, the combination of low reflectivities observed by PR along with light rain identified by CloudSat in the surrounding pixels suggests the presence of smaller drops. This would in turn lead to an underestimate by the PR retrieval, which combined with an overestimate by the CPR retrieval due to enhanced cloud water could explain the large differences between the two radar rain retrievals. Given the lifecycle issues and the idealized nature of the

simulations, however, this hypothesis is neither fully supported nor disputed by the model results.

6. Summary and Conclusions

[31] A combination of coincident satellite observations from TRMM PR, TMI, and CloudSat CPR are used along with CRM simulations to investigate the impact of high sulfate aerosol concentrations on precipitating clouds off the coast of China in order to explain large differences in seasonal mean rainfall estimates between TMI and PR. Because rainfall retrievals from TMI, PR, and CPR respond differently to changes in DSD, significant deviations from the assumed DSD will lead to different errors in the various estimates. As a result, coincident TRMM/CloudSat observations east of Japan from 2 December 2006, which show excellent agreement in both rain area and intensity from the three satellite rain retrievals, suggests a DSD that is consistent with the distributions assumed by the retrieval algorithms. This is clearly not the case, however, for coincident observations southeast of Japan from 3 April 2007, which corresponds to an environment with high concentrations of sulfate aerosols. In this case, large differences in both the rain area and rainfall intensity are consistent with the presence of widespread light rain/drizzle containing relatively small drops that are missed by the PR because of its lack of sensitivity. This result is confirmed along the CloudSat ground track where the CPR retrieval, which is highly sensitive to the onset of rain, shows good agreement with the TMI rain area. Since meteorological considerations cannot be isolated from the influence of aerosols on the observed cloud microphysics, idealized CRM simulations initialized for the 3 April 2007 case are run with varying amounts of aerosols while keeping the synoptic forcing fixed. The CRM results suggest an increase in the LWP threshold corresponding to the onset of rain for high aerosol concentrations. For the case examined here, however, the observations suggest that this effect is relatively small compared to the area of light rain that falls below the sensitivity of the PR. It is nevertheless important to note that changes in the rain/no rain threshold due to aerosols may have important implications for rainfall detection from passive microwave sensors over this region.

[32] The CRM simulations indicate not only a delay in the onset of rain, but also an increase in the ratio of cloud water to rainwater for the high aerosol cases. Such an increase in the amount of cloud water can lead to an overestimate of the rain rate by both the attenuation-based CPR and the emission-based TMI retrievals. This is because both the TMI emission signal and the CPR attenuation respond primarily to changes in total water. Since the amount of cloud water is prescribed in the algorithms on the basis of relationships that do not account for aerosols, any increase in the cloud water over the assumed value will lead to an overestimate in the total rainwater and thus the rain rate. Similarly, a decrease in the mean drop size, which is consistent with both the low PR reflectivities observed in the 3 April 2007 case as well as the light rain/drizzle observed by the CPR in the surrounding pixels, would lead to an underestimate of the rain rate by PR. The impact of aerosols on the mean raindrop size in the CRM simulations is somewhat mixed with an initial decrease in drop size followed by an overall increase relative to the nonpolluted cases. Because the satellite observations provide a snapshot, with no context as to the corresponding position in the lifecycle of the system, fully determining the factors leading to differences in the rain estimates may ultimately require intensive observations from a field program where the evolution of a system over its complete lifecycle can be observed. The satellite observations do provide compelling evidence, however, for the presence of widespread light rain/drizzle in the 3 April 2007 case. Furthermore, although the CRM simulations are from a single case and do not include the advection of aerosols into the system, the model results indicate several changes in the high aerosol cases that merit further investigation. These include an increase in the amount of cloud water prior to the onset of rain, an increase in the ratio of cloud water to rainwater in the developed systems, and a decrease in evaporation of raindrops resulting in an overall increase in the total accumulated rainfall at the surface.

[33] Rather than attempting to assign discrepancies to failures of any one sensor, an impossible task given the lack of any available "truth," the point here is simply that there is a wealth of information in the rainfall differences themselves that may serve as a proxy for detecting potential aerosol impacts on global scales. It is also important to reiterate that the discrepancies shown in the 3 April 2007 case are not an isolated event, but occur frequently over the East China Sea and surrounding regions. The nature of the CloudSat and TRMM orbits is such that the number of cases from which statistics can be drawn is somewhat limited, however, Figure 1 suggests that similar effects dominate the rainfall characteristics in the East China Sea region, particularly during the DJF and MAM seasons. Indeed, the frequency of detection of rainfall from TMI for the region just off the coast of China during DJF 1999/2000 is approximately twice that of the PR and it accounts for $\sim$50% of the total TMI estimated rainfall in this region. While the impacts are the largest just off the coast, they are clearly apparent, albeit less dramatic, over a broad region extending well off the coast, particularly during MAM. As a result, the high aerosol case examined here highlight the potential for using this combination of satellite sensors along with CRM simulations to investigate the impact of aerosols on rainfall and the associated satellite estimates, especially as additional data is collected.

[34] **Acknowledgments.** The authors would like to thank John Haynes for providing the CloudSat rainfall estimates along with his comments and expertise. Also, thanks to Christian Kummerow and Steven Rutledge for their comments and to Toshihiko Takemura at Kyushu University for providing the SPRINTARS data. Funding for this work was provided under NASA grants NNX07AD81G and NNX07AR97G and NOAA grant NAS5–99237.

References

Albrecht, B. (1989), Aerosols, cloud microphysics, and fractional cloudiness, *Science*, *245*, 1227–1230, doi:10.1126/science.245.4923.1227.

Altaratz, O., I. Koren, T. Reisin, A. Kostinski, G. Feingold, Z. Levin, and Y. Yin (2007), Aerosols' influence on the interplay between condensation, evaporation and rain in warm cumulus cloud, *Atmos. Chem. Phys. Discuss.*, *7*, 1–28.

Austin, R. T., and G. L. Stephens (2001), Retrieval of stratus cloud microphysical parameters using millimeter-wave radar and visible optical depth in preparation for CloudSat, 1, Algorithm formulation, *J. Geophys. Res.*, *106*(D22), 28,233–28,242, doi:10.1029/2000JD000293.

Berg, W., T. L'Ecuyer, and C. Kummerow (2006), Rainfall climate regimes: The relationship of regional TRMM rainfall biases to the environment, *J. Appl. Meteorol. Climatol.*, *45*(3), 434–454, doi:10.1175/JAM2331.1.

Carrio, G. G., S. C. van den Heever, and W. R. Cotton (2007), Impacts of nucleating aerosol on anvil-cirrus clouds: A modeling study, *Atmos. Res.*, *84*, 111–131, doi:10.1016/j.atmosres.2006.06.002.

Cotton, W. R., et al. (2003), RAMS 2001: Current status and future directions, *Meteorol. Atmos. Phys.*, *82*, 5–29, doi:10.1007/s00703-001-0584-9.

Elsaesser, G. S., and C. D. Kummerow (2008), Towards a fully parametric retrieval of the non-raining parameters over the global oceans, *J. Appl. Meteorol. Climatol.*, in press.

Feingold, G., S. Tzivion, and Z. Levin (1988), Evolution of raindrop spectra. Part I: Solution to the stochastic collection/breakup equation using the method of moments, *J. Atmos. Sci.*, *45*(22), 3387–3399, doi:10.1175/1520-0469(1988)045<3387:EORSPI>2.0.CO;2.

Givati, A., and D. Rosenfeld (2004), Quantifying precipitation suppression due to air pollution, *J. Appl. Meteorol.*, *43*, 1038–1056, doi:10.1175/1520-0450(2004)043<1038:QPSDTA>2.0.CO;2.

Iguchi, T., T. Kozu, R. Meneghini, J. Awaka, and K. Okamoto (2000), Rain-profiling algorithm for the TRMM precipitation radar, *J. Appl. Meteorol.*, *39*, 2038–2052, doi:10.1175/1520-0450(2001)040<2038:RPAFTT>2.0.CO;2.

Ishizaka, Y., et al. (2003), The effect of air-pollutants on the microphysical properties of clouds over the sea off the southwest of Kyushu in Japan, in *Findings and Current Problems in the Asian Particle Environmental Change Studies: 2003, JST/CREST/APEX 2003 Interim Report*, pp. 103–116, Univ. of Tokyo, Tokyo.

Jiang, H., H. Xue, A. Teller, G. Feingold, and Z. Levin (2006), Aerosol effects on the lifetime of shallow cumulus, *Geophys. Res. Lett.*, *33*, L14806, doi:10.1029/2006GL026024.

Kaufman, Y. J., I. Koren, L. A. Remer, D. Rosenfeld, and Y. Rudich (2005), The effect of smoke, dust and pollution aerosol on shallow cloud development over the Atlantic Ocean, *Proc. Natl. Acad. Sci. U.S.A.*, *102*(32), 11,207–11,212, doi:10.1073/pnas.0505191102.

Khain, A. D., D. Rosenfeld, and A. Pokrovsky (2005), Aerosol impact on the dynamics and microphysics of deep convective clouds, *Q. J. R. Meteorol. Soc.*, *131*, 2639–2663, doi:10.1256/qj.04.62.

Kollias, P., E. E. Clothiaux, M. A. Miller, B. A. Albrecht, G. L. Stephens, and T. P. Ackerman (2007), Millimeter-wavelength radars: New frontier in atmospheric cloud and precipitation research, *Bull. Am. Meteorol. Soc.*, *88*(10), 1608–1624, doi:10.1175/BAMS-88-10-1608.

Kummerow, C., W. Barnes, T. Kozu, J. Shiue, and J. Simpson (1998), The Tropical Rainfall Measuring Mission (TRMM) sensor package, *J. Atmos. Oceanic Technol.*, *15*, 809–817, doi:10.1175/1520-0426(1998)015<0809:TTRMMT>2.0.CO;2.

Kummerow, C., et al. (2000), The status of the Tropical Rainfall Measuring Mission (TRMM) after two years in orbit, *J. Appl. Meteorol.*, *39*, 1965–1982, doi:10.1175/1520-0450(2001)040<1965:TSOTTR>2.0.CO;2.

Kummerow, C., Y. Hong, W. S. Olson, S. Yang, R. F. Adler, J. McCollum, R. Ferraro, G. Petty, D. B. Shin, and T. T. Wilheit (2001), The evolution of the Goddard profiling algorithm (GPROF) for rainfall estimation from passive microwave sensors, *J. Appl. Meteorol.*, *40*, 1801–1820, doi:10.1175/1520-0450(2001)040<1801:TEOTGP>2.0.CO;2.

L'Ecuyer, T. S., and G. L. Stephens (2002), An estimation-based precipitation retrieval algorithm for attenuating radars, *J. Appl. Meteorol.*, *41*, 272–285, doi:10.1175/1520-0450(2002)041<0272:AEBPRA>2.0.CO;2.

Lin, J. C., T. Matsui, R. A. Pielke Sr., and C. Kummerow (2006), Effects of biomass burning-derived aerosols on precipitation and clouds in the Amazon Basin: A satellite-based empirical study, *J. Geophys. Res.*, *111*, D19204, doi:10.1029/2005JD006884.

Marshall, J. S., and W. M. Palmer (1948), The distributions of raindrops with size, *J. Meteorol.*, *9*, 327–332.

Matrosov, S. Y. (2007), Potential for attenuation-based estimations of rainfall rate from CloudSat, *Geophys. Res. Lett.*, *34*, L05817, doi:10.1029/2006GL029161.

Matsui, T., H. Masunaga, R. A. Pielke Sr., and W.-K. Tao (2004), Impact of aerosols and atmospheric thermodynamics on cloud properties within the climate system, *Geophys. Res. Lett.*, *31*, L06109, doi:10.1029/2003GL019287.

Matsui, T., H. Masunaga, S. M. Kreidenweis, R. A. Pielke Sr., W.-K. Tao, M. Chin, and Y. Kaufman (2006), Satellite-based assessment of global warm cloud properties associated with aerosols, atmospheric stability, and diurnal cycle, *J. Geophys. Res.*, *111*, D17204, doi:10.1029/2005JD006097.

Meyers, M. P., R. L. Walko, J. Y. Harrington, and W. R. Cotton (1997), New RAMS cloud microphysics parameterization. Part II: The two-moment scheme, *Atmos. Res.*, *45*, 3–39, doi:10.1016/S0169-8095(97)00018-5.

Pielke, R. A., et al. (1992), A comprehensive meteorological modeling system–RAMS, *Meteorol. Atmos. Phys.*, *49*, 69–91, doi:10.1007/BF01025401.

Rosenfeld, D. (1999), TRMM observed first direct evidence of smoke from forest fires inhibiting rainfall, *Geophys. Res. Lett.*, *26*, 3105–3108, doi:10.1029/1999GL006066.

Rosenfeld, D., and I. M. Lensky (1998), Spaceborne sensed insights into precipitation formation processes in continental and maritime clouds, *Bull. Am. Meteorol. Soc.*, *79*, 2457–2476, doi:10.1175/1520-0477(1998)079<2457:SBIIPF>2.0.CO;2.

Saleeby, S. M., and W. R. Cotton (2004), A large-droplet mode and prognostic number concentration of cloud droplets in the Colorado State Univ. Regional Atmospheric Modeling System (RAMS). Part I: Module descriptions and supercell test simulations, *J. Appl. Meteorol.*, *43*, 182–195, doi:10.1175/1520-0450(2004)043<0182:ALMAPN>2.0.CO;2.

Schumacher, C., and R. A. Houze (2000), Comparison of radar data from the TRMM satellite and Kwajalein oceanic validation site, *J. Appl. Meteorol.*, *39*, 2151–2164, doi:10.1175/1520-0450(2001)040<2151:CORDFT>2.0.CO;2.

Stephens, G. L., et al. (2002), The CloudSat mission and the A-Train, *Bull. Am. Meteor. Soc.*, *83*, 1771–1790.

Takemura, T., H. Okamoto, Y. Maruyama, A. Numaguti, A. Higurashi, and T. Nakajima (2000), Global three-dimensional simulation of aerosol optical thickness distribution of various origins, *J. Geophys. Res.*, *105*, 17,853–17,873, doi:10.1029/2000JD900265.

Takemura, T., T. Nakajima, O. Dubovik, B. N. Holben, and S. Kinne (2002), Single-scattering albedo and radiative forcing of various aerosol species with a global three-dimensional model, *J. Clim.*, *15*, 333–352, doi:10.1175/1520-0442(2002)015<0333:SSAARF>2.0.CO;2.

Takemura, T., T. Nozawa, S. Emori, T. Y. Nakajima, and T. Nakajima (2005), Simulation of climate response to aerosol direct and indirect effects with aerosol transport-radiation model, *J. Geophys. Res.*, *110*, D02202, doi:10.1029/2004JD005029.

Twomey, S. (1974), Pollution and the planetary albedo, *Atmos. Environ.*, *8*, 1251–1256, doi:10.1016/0004-6981(74)90004-3.

Twomey, S. (1977), The influence of pollution on the short-wave albedo of clouds, *J. Atmos. Sci.*, *34*, 1149–1152, doi:10.1175/1520-0469(1977)034<1149:TIOPOT>2.0.CO;2.

van den Heever, S. C., and W. R. Cotton (2007), Urban aerosol impacts on downwind convective storms, *J. Appl. Meteorol.*, *46*, 828–850, doi:10.1175/JAM2492.1.

van den Heever, S. C., G. G. Carrio, W. R. Cotton, P. J. DeMott, and A. J. Prenni (2006), Impacts of nucleating aerosol on Florida storms. Part I: Mesoscale simulations, *J. Atmos. Sci.*, *63*, 1752–1775, doi:10.1175/JAS3713.1.

Xue, H., and G. Feingold (2006), Large eddy simulations of tradewind cumuli: Investigation of aerosol indirect effects, *J. Atmos. Sci.*, *63*, 1605–1622, doi:10.1175/JAS3706.1.

Zhao, C., X. Tie, and Y. Lin (2006), A possible positive feedback of reduction of precipitation and increase in aerosols over eastern central China, *Geophys. Res. Lett.*, *33*, L11814, doi:10.1029/2006GL025959.

W. Berg, T. L'Ecuyer, and S. van den Heever, Department of Atmospheric Science, Colorado State University, Fort Collins, CO 80523-1371, USA. (berg@atmos.colostate.edu)